

# Potential enthalpic energy of water in oils exploited to control supramolecular structure

Nathan J. Van Zee<sup>1</sup>, Beatrice Adelizzi<sup>1</sup>, Mathijs F. J. Mabesoone<sup>1</sup>, Xiao Meng<sup>1</sup>, Antonio Aloi<sup>1,2</sup>, R. Helen Zha<sup>1</sup>, Martin Lutz<sup>3</sup>, Ivo A. W. Filot<sup>1,4</sup>, Anja R. A. Palmans<sup>1</sup> & E. W. Meijer<sup>1\*</sup>

**Water directs the self-assembly of both natural<sup>1,2</sup> and synthetic<sup>3–9</sup> molecules to form precise yet dynamic structures. Nevertheless, our molecular understanding of the role of water in such systems is incomplete, which represents a fundamental constraint in the development of supramolecular materials for use in biomaterials, nanoelectronics and catalysis<sup>10</sup>. In particular, despite the widespread use of alkanes as solvents in supramolecular chemistry<sup>11,12</sup>, the role of water in the formation of aggregates in oils is not clear, probably because water is only sparingly miscible in these solvents—typical alkanes contain less than 0.01 per cent water by weight at room temperature<sup>13</sup>. A notable and unused feature of this water is that it is essentially monomeric<sup>14</sup>. It has been determined previously<sup>15</sup> that the free energy cost of forming a cavity in alkanes that is large enough for a water molecule is only just compensated by its interaction with the interior of the cavity; this cost is therefore too high to accommodate clusters of water. As such, water molecules in alkanes possess potential enthalpic energy in the form of unrealized hydrogen bonds. Here we report that this energy is a thermodynamic driving force for water molecules to interact with co-dissolved hydrogen-bond-based aggregates in oils. By using a combination of spectroscopic, calorimetric, light-scattering and theoretical techniques, we demonstrate that this interaction can be exploited to modulate the structure of one-dimensional supramolecular polymers.**

We discovered the importance of this principle in exploring the self-assembly of enantiopure **1** (Fig. 1a). In the bulk, **1** forms helical liquid crystalline structures at 20 °C with dimensions typical of one-dimensional aggregates<sup>16</sup> (Extended Data Fig. 1). As seen from super-resolution fluorescence and atomic force microscopy (AFM) images (Fig. 1b, c, respectively, and Extended Data Fig. 2), **1** also forms one-dimensional aggregates when diluted in oils such as methylcyclohexane (MCH). At micromolar concentrations in MCH, aggregates of **1** exhibit a preferred helicity, as observed by variable temperature circular dichroism (VT-CD) spectroscopy. However, surprisingly, the sign of the Cotton effect depends on the temperature of the solution. Early experiments were marred by seemingly inexplicable irreproducibility of the critical temperatures at which the transitions between these different helicities occur. We discovered the underlying cause by unexpectedly drying a solution of **1** in the nitrogen-purged atmosphere of the sample holder of the CD spectrometer (see Extended Data Fig. 3 for an analogous experiment). This dried sample no longer exhibited the distinctive helical transitions.

It became clear that unintended fluctuations in water content accounted for these initial inconsistencies, which motivated us to investigate the effect of water in supramolecular aggregation in oils in general, and its role in determining the helicity of aggregates of **1** in particular. We assessed the self-assembly of **1** in MCH ([**1**] = 30 μM) with 35 p.p.m. water (measured by Karl Fischer titration) by VT-CD and ultraviolet spectroscopies between 95 °C and 5 °C while cooling at 60 °C h<sup>-1</sup> (Fig. 1d). At temperatures greater than 81 °C, **1** exhibits an ultraviolet absorption maximum at 221 nm and no CD signal,

which indicates that it is molecularly dissolved. Upon cooling to 81 °C, **1** self-assembles to form chiral aggregates, **A**, which have a positive bisignate Cotton effect at 258 nm along with a blue-shifted ultraviolet spectrum. Cooling from 81 °C to 29 °C results in a rapid increase in intensity of the CD signal, which suggests that **A** forms through a cooperative supramolecular polymerization of **1**. An unprecedentedly abrupt transition is then observed when the solution is cooled from 29 °C to 27 °C, resulting in the conversion of **A** into a second chiral aggregate, **B**, with a positive Cotton effect at 250 nm and essentially the same ultraviolet spectrum as that of **A**. Continued cooling to 21 °C results in a slight decrease in the intensity of the CD signal of **B**, but cooling just below 21 °C gives rise to the rapid transformation of **B** into a third chiral aggregate, **C**, which exhibits a negative Cotton effect at 238 nm; further cooling does not initiate additional helical transitions.

Using VT-CD spectroscopy, we next investigated how the concentrations of both **1** and water affect the critical temperatures of these transitions. The progress of self-assembly was followed by monitoring the intensity of the Cotton effect at 258 nm as solutions were cooled from 95 °C to -5 °C at 60 °C h<sup>-1</sup>. The formation of **A** is dependent on the concentration of **1**, as its critical elongation temperature decreases from 91 °C to 70 °C as the concentration of **1** decreases from 59 μM to 10 μM (Fig. 1e). A van 't Hoff analysis reveals that the enthalpy of elongation is -86 kJ (mol **1**)<sup>-1</sup> (Extended Data Fig. 4a), consistent with this process being driven by the formation of four hydrogen bonds per molecule of **1**<sup>17,18</sup>. The transformations of **A** → **B** and **B** → **C** are not sensitive to the concentration of **1** and take place over a narrow temperature range. Moreover, these transitions exhibit a marked dependence on the concentration of co-dissolved water (Fig. 1f). At 47 p.p.m. water, **A** → **B** and **B** → **C** occur at 35 °C and 25 °C, respectively. As the water content decreases, they occur at progressively lower temperatures, which suggests that water binds to the structures of **B** and **C**. Van 't Hoff plots reveal that the enthalpies of **A** → **B** and **B** → **C** are about -21 and -26 kJ (mol H<sub>2</sub>O)<sup>-1</sup>, respectively, which indicates that the enthalpic driving force for water to bind is essentially the same in each transition (Extended Data Fig. 4b, c). At 8 p.p.m. water, only **A** is formed even after cooling to -5 °C, but it should be noted that water is still present in over tenfold molar excess relative to **1**.

To further establish that water molecules bind to **B** and **C**, we studied each aggregate by Fourier-transform infrared (FTIR) spectroscopy. **A**, **B** and **C** were all produced at 20 °C ([**1**] = 2.0 mM) simply by modulating the water content of the solution (Fig. 2a). For instance, **B** forms at 20 °C when **1** is polymerized in MCH that is used as received; however, when **1** is polymerized in MCH that has been dried with activated molecular sieves, **A** forms instead at 20 °C. FTIR spectroscopy reveals that **A**, **B** and **C** all exhibit red-shifted N-H stretching, red-shifted amide I bands and blue-shifted amide II bands compared to molecularly dissolved **1** in chloroform, typical of hydrogen-bond-based aggregation of carboxamides (Fig. 2b). Of particular interest is the fact that the FTIR spectrum of **B** features a shoulder at 3,520 cm<sup>-1</sup> that is not observed for **A**, and this shoulder appears to evolve into a new band at 3,558 cm<sup>-1</sup> in the

<sup>1</sup>Institute for Complex Molecular Systems, Laboratory of Macromolecular and Organic Chemistry, Eindhoven University of Technology, Eindhoven, The Netherlands. <sup>2</sup>Laboratory of Self-Organizing Soft Matter, Eindhoven University of Technology, Eindhoven, The Netherlands. <sup>3</sup>Crystal and Structural Chemistry, Bijvoet Center for Biomolecular Research, Utrecht University, Utrecht, The Netherlands. <sup>4</sup>Inorganic Materials Chemistry, Eindhoven University of Technology, Eindhoven, The Netherlands. \*e-mail: e.w.meijer@tue.nl

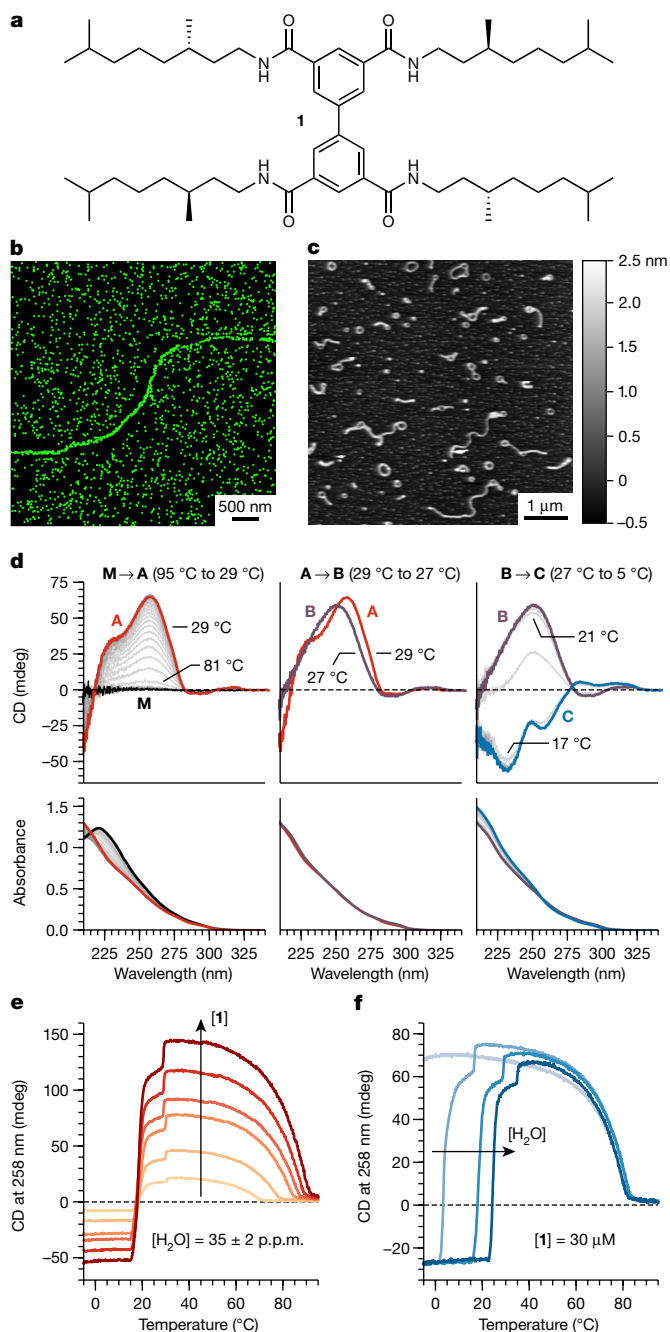


**Fig. 1 | Self-assembly of **1** in MCH.** **a**, Chemical structure of enantiopure **1**. **b**, Super-resolution fluorescence microscopy image of a fibre of **1**. **c**, AFM image of fibres of **1**. **d**, CD and ultraviolet spectra of molecularly dissolved **1** (**M**), **A**, **B** and **C** while cooling a solution of **1** in MCH ( $[1] = 30 \mu\text{M}$ ,  $[\text{H}_2\text{O}] = 35 \pm 2 \text{ p.p.m.}$ ). **e**, VT-CD cooling experiments in which the concentration of **1** was varied while the water content was held constant ( $[1] = 59 \mu\text{M}$  (darkest shade),  $49 \mu\text{M}$ ,  $40 \mu\text{M}$ ,  $33 \mu\text{M}$ ,  $20 \mu\text{M}$  and  $10 \mu\text{M}$  (lightest shade);  $[\text{H}_2\text{O}] = 35 \pm 2 \text{ p.p.m.}$ ). **f**, VT-CD cooling experiments in which the water content was varied while the concentration of **1** was held constant ( $[\text{H}_2\text{O}] = 47 \pm 3 \text{ p.p.m.}$  (darkest shade),  $35 \pm 2 \text{ p.p.m.}$ ,  $24 \pm 4 \text{ p.p.m.}$ ,  $8 \pm 1 \text{ p.p.m.}$  (lightest shade);  $[1] = 30 \mu\text{M}$ ). All water content measurements are reported as mean  $\pm$  s.d. ( $n = 2$ ).

spectrum of **C**. On the basis of previous studies<sup>19,20</sup>, the frequencies of these bands are consistent with O–H stretching vibrations of water molecules that are engaged in hydrogen bonding through both of their OH groups. Considered together with the accompanying shifts of the N–H stretching band and those of the amide I and amide II bands exhibited by **B** and **C**, these measurements indicate that these structures are formed through the incorporation of water.

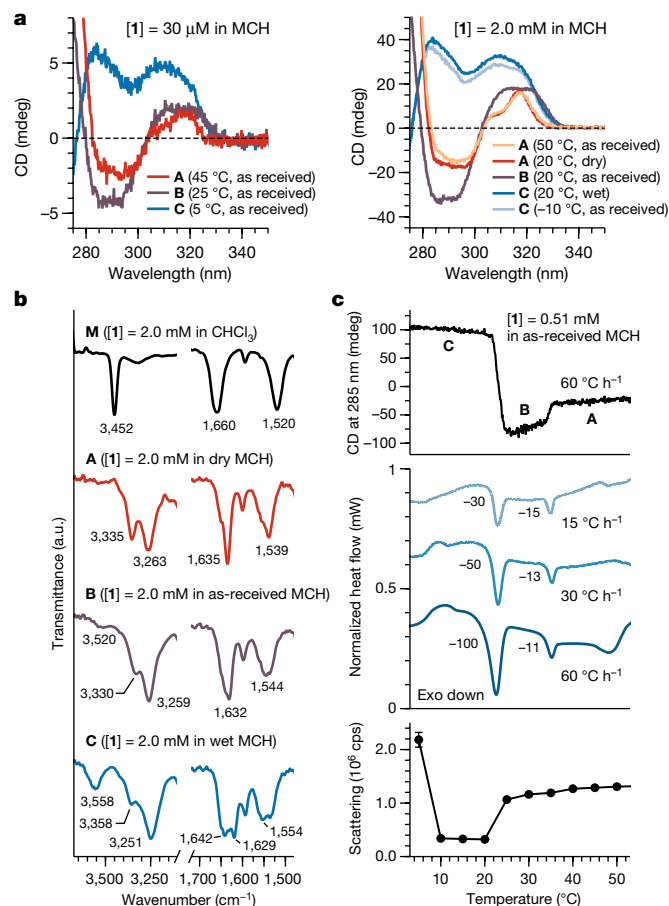


**Fig. 2 | Characterization of aggregates of **1** by CD spectroscopy, FTIR spectroscopy, micro-DSC and light scattering.** **a**, Diagnostic region of the CD spectra of **A**, **B** and **C**, with the concentration of **1** at  $30 \mu\text{M}$  (left,  $l = 10 \text{ mm}$ ) and  $2.0 \text{ mM}$  (right,  $l = 1 \text{ mm}$ ). **b**, Comparison of the O–H and N–H stretching (left) and the amide I and amide II (right) regions of the FTIR spectra of **M**, **A**, **B** and **C** (labels in  $\text{cm}^{-1}$ ). **c**, CD signal (top), micro-DSC curves (middle, labels in  $\text{kJ} (\text{mol } 1)^{-1}$ ) and light-scattering counts (bottom, mean  $\pm$  s.d. ( $n = 5$ )) are shown) acquired while cooling a solution of **1** in MCH.

If there is a net increase in the number of hydrogen bonds formed, **A**  $\rightarrow$  **B** and **B**  $\rightarrow$  **C** are expected to evolve heat assuming minimal thermal contributions from changes in solvation. We characterized a  $0.51 \text{ mM}$  solution of **1** by both VT-CD spectroscopy and micro-differential scanning calorimetry (micro-DSC) between  $60 \text{ }^\circ\text{C}$  and  $0 \text{ }^\circ\text{C}$  (Fig. 2c, top and middle) and detected exothermic transitions that clearly correspond to **A**  $\rightarrow$  **B** and **B**  $\rightarrow$  **C**, respectively, as well as a broad endothermic transition that occurs just below the critical temperature of **B**  $\rightarrow$  **C**. Whereas the enthalpy of the **A**  $\rightarrow$  **B** transition is insensitive to the scan rate, that of the **B**  $\rightarrow$  **C** transition becomes less exothermic from  $-100$  to  $-30 \text{ kJ} (\text{mol } 1)^{-1}$  as the scan rate is decreased from  $60$  to  $15 \text{ }^\circ\text{C h}^{-1}$ , which appears to result from the endothermic transition concomitantly shifting to higher temperatures and overlapping more with **B**  $\rightarrow$  **C**. We discovered that **C** scatters less light than **B** just below the critical temperature of **B**  $\rightarrow$  **C** (Fig. 2c, bottom), which suggests that the endothermic transition corresponds to fibre fragmentation reactions. These processes are all reversible, although hysteresis is observed between **B**  $\rightarrow$  **C** and **C**  $\rightarrow$  **B** (Extended Data Figs. 5, 6, respectively), which is indicative of pathway complexity<sup>21</sup>.

An important question concerns how much water is bound to **B** and **C**. To answer this question, we constructed a thermodynamic model consisting of three competing, cooperative supramolecular polymerization pathways<sup>22</sup> (Fig. 3a; see Supplementary Information for details) that enables the derivation of equations for the free energy of elongation of **B** and **C** (Supplementary Information equations (13), (18)). Using

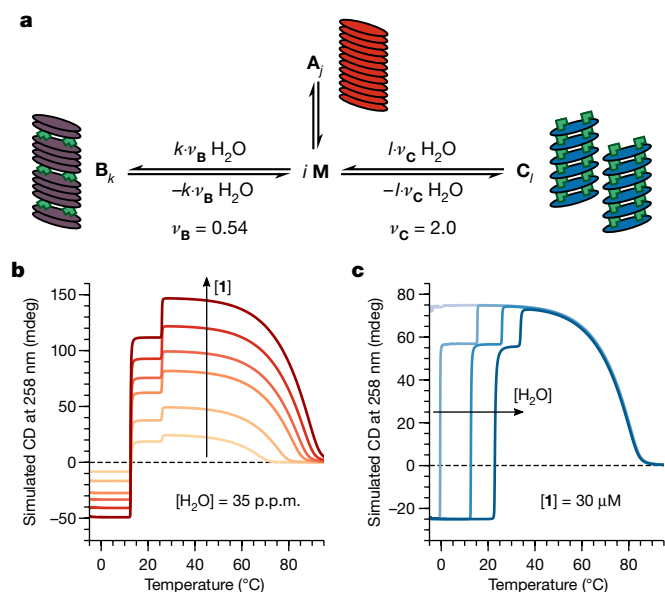


**Fig. 3 | Thermodynamic model for the formation of A, B and C.**

**a**, Schematic representation of three cooperative, competitive pathways. The variables  $j$ ,  $k$  and  $l$  correspond to the degrees of polymerization of A, B and C, respectively. The coloured discs represent aggregated monomer units, and the green blocks represent water molecules. **b**, Simulated VT-CD cooling curves in which the concentration of **1** was varied while the water content was held constant ( $[1] = 59 \mu\text{M}$  (darkest shade),  $49 \mu\text{M}$ ,  $40 \mu\text{M}$ ,  $33 \mu\text{M}$ ,  $20 \mu\text{M}$  and  $10 \mu\text{M}$  (lightest shade);  $[\text{H}_2\text{O}] = 35 \text{ p.p.m.}$ ). **c**, Simulated VT-CD cooling curves in which the water content was varied while the concentration of **1** was held constant ( $[\text{H}_2\text{O}] = 47 \text{ p.p.m.}$  (darkest shade),  $35 \text{ p.p.m.}$ ,  $24 \text{ p.p.m.}$  and  $8 \text{ p.p.m.}$  (lightest shade);  $[1] = 30 \mu\text{M}$ ).

the enthalpy of elongation of A (Extended Data Fig. 4a) and the calorimetric enthalpies of  $\text{A} \rightarrow \text{B}$  and  $\text{B} \rightarrow \text{C}$  (Fig. 2c), as well as the transition temperatures of  $\text{A} \rightarrow \text{B}$  and  $\text{B} \rightarrow \text{C}$  at different concentrations of water

(Fig. 1f), these equations are used to calculate stoichiometries of water for B and C (that is,  $\nu_B$  and  $\nu_C$  in Fig. 3a) of 0.54 and 2.0, respectively. These calculations also yield values for the entropies of elongation of B and C; both values agree with those reported for related supramolecular polymerizations<sup>18,23</sup>. Incorporation of these parameters into a temperature-dependent version of the model enables us to simulate the experimental VT-CD curves presented in Fig. 1e, f with a high level of accuracy (Fig. 3b, c, respectively). Although the molecular structures of B and C remain elusive, we used density functional theory to construct models based on the geometrical parameters obtained from a crystal structure of a chemical analogue of **1** (Extended Data Fig. 7). These models confirm that the incorporation of several water molecules into one-dimensional aggregates of biphenyl tetracarboxamide molecules results in a stable structure<sup>24,25</sup> (Extended Data Fig. 8).

The action of water in oils that is demonstrated here is a result of the potential enthalpic energy of molecularly dissolved water, which is an often overlooked manifestation of hydrophobic effects<sup>26,27</sup>. Although hints that point towards these underlying effects have existed for decades<sup>14,15,28,29</sup>, the present results illustrate the profound molecular consequences of binding even a minuscule amount of water, which prompted us to investigate the effect of water content on the structure of other supramolecular aggregates in oils. We chose to re-examine the self-assembly of triarylaminines **4** and **5** (Fig. 4a, top). Both form helical aggregates that exhibit changes in helicity as a function of temperature<sup>30</sup>. VT-CD spectroscopic measurements reveal that the helicities of the resulting aggregates in MCH are sensitive to the concentration of water (Fig. 4b, c), which suggests that water molecules directly interact with these structures as well.

We also investigated the effect of water content on the self-assembly of chiral benzene tricarboxamide **6** (Fig. 4a, bottom), which has been the subject of many previous studies<sup>11</sup>. Although variation of the water content does not affect their helicity, aggregates of **6** prepared in wet MCH scatter more light than fibres formed in dry MCH (Extended Data Fig. 9a). Measurements by AFM suggest an important role for water in modulating the lateral interaction between fibres based on **6**.

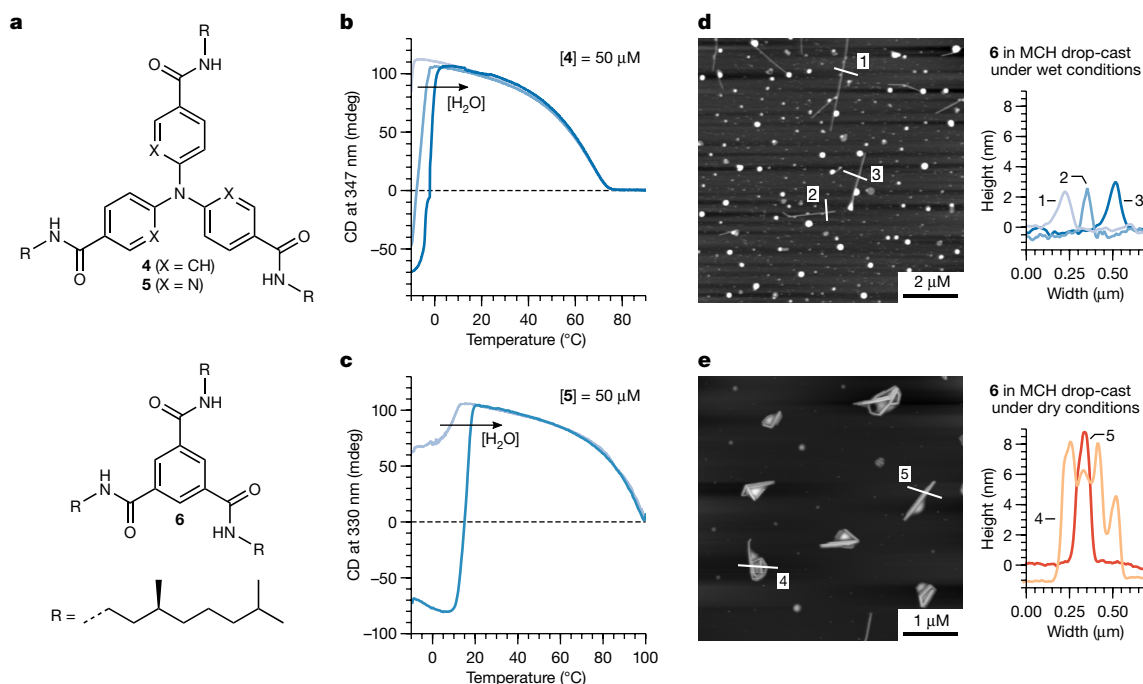


**Fig. 4 | Influence of water on the self-assembly of 4, 5 and 6 in MCH.** **a**, Chemical structures of enantiopure **4**, **5** and **6**. **b**, VT-CD cooling experiments in which the water content was varied while the concentration of **4** was held constant ( $[\text{H}_2\text{O}] = 60 \pm 4 \text{ p.p.m.}$  (darkest shade),  $20 \pm 4 \text{ p.p.m.}$  and  $5 \pm 3 \text{ p.p.m.}$  (lightest shade);  $[4] = 50 \mu\text{M}$ ; cooling rate =  $60 \text{ }^\circ\text{C h}^{-1}$ ). **c**, VT-CD cooling experiments in which the water content was varied while the concentration of **5** was held constant

( $[\text{H}_2\text{O}] = 29 \pm 2 \text{ p.p.m.}$  (darker shade) and  $17 \pm 2 \text{ p.p.m.}$  (lighter shade);  $[5] = 50 \mu\text{M}$ ; cooling rate =  $15 \text{ }^\circ\text{C h}^{-1}$ ). All water content measurements in **b** and **c** are reported as mean  $\pm$  s.d. ( $n = 2$ ). **d**, AFM image (left) and height profiles (right) of a sample of **6** prepared in a water-saturated environment. **e**, AFM image (left) and height profiles (right) of a sample of **6** prepared in a glovebox. The difference in morphology observed for aggregates of **6** presented in **d** and **e** was duplicated in our laboratory.

Single-chain fibres are observed when **6** is drop-cast under wet conditions (Fig. 4d and Extended Data Fig. 9b), whereas coils of several chains are detected in samples prepared under dry conditions (Fig. 4e and Extended Data Fig. 9c). We propose that many other unidentified structural transitions observed in hydrogen-bond-based aggregation in oils arise from fundamental interactions with monomeric water molecules in these highly apolar solvents.

### Online content

Any Methods, including any statements of data availability and Nature Research reporting summaries, along with any additional references and Source Data files, are available in the online version of the paper at <https://doi.org/10.1038/s41586-018-0169-0>.

Received: 16 July 2017; Accepted: 16 March 2018;

Published online: 30 May 2018

- Nagornova, N. S., Rizzo, T. R. & Boyarkin, O. V. Interplay of intra- and intermolecular H-bonding in a progressively solvated macrocyclic peptide. *Science* **336**, 320–323 (2012).
- Umena, Y., Kawakami, K., Shen, J. R. & Kamiya, N. Crystal structure of oxygen-evolving photosystem II at a resolution of 1.9 Å. *Nature* **473**, 55–60 (2011).
- Berl, V., Huc, I., Khoury, R. G., Krische, M. J. & Lehn, J. M. Interconversion of single and double helices formed from synthetic molecular strands. *Nature* **407**, 720–723 (2000).
- Hirschberg, J. H. K. K. et al. Helical self-assembled polymers from cooperative stacking of hydrogen-bonded pairs. *Nature* **407**, 167–170 (2000).
- Hartgerink, J. D., Beniash, E. & Stupp, S. I. Self-assembly and mineralization of peptide-amphiphile nanofibers. *Science* **294**, 1684–1688 (2001).
- Jain, S. & Bates, F. S. On the origins of morphological complexity in block copolymer surfactants. *Science* **300**, 460–464 (2003).
- Johnson, R. S., Yamazaki, T., Kovalenko, A. & Fenniri, H. Molecular basis for water-promoted supramolecular chirality inversion in helical rosette nanotubes. *J. Am. Chem. Soc.* **129**, 5735–5743 (2007).
- Appel, E. A. et al. Supramolecular cross-linked networks via host-guest complexation with cucurbit[8]uril. *J. Am. Chem. Soc.* **132**, 14251–14260 (2010).
- Arazoe, H. et al. An autonomous actuator driven by fluctuations in ambient humidity. *Nat. Mater.* **15**, 1084–1089 (2016).
- Aida, T., Meijer, E. W. & Stupp, S. I. Functional supramolecular polymers. *Science* **335**, 813–817 (2012).
- De Greef, T. F. et al. Supramolecular polymerization. *Chem. Rev.* **109**, 5687–5754 (2009).
- Liu, M., Zhang, L. & Wang, T. Supramolecular chirality in self-assembled systems. *Chem. Rev.* **115**, 7304–7397 (2015).
- Riddick, J. A., Bunger, W. B. & Sakano, T. K. *Organic Solvents, Physical Properties and Methods of Purification*. (John Wiley & Sons, New York, 1986).
- Christian, S. D., Taha, A. A. & Gash, B. W. Molecular complexes of water in organic solvents and in the vapour phase. *Q. Rev. Chem. Soc.* **24**, 20–36 (1970).
- Wolfenden, R. & Radzicka, A. On the probability of finding a water molecule in a nonpolar cavity. *Science* **265**, 936–937 (1994).
- Fitić, C. F. et al. Polar switching in trialkylbenzene-1,3,5-tricarboxamides. *J. Phys. Chem. B* **116**, 3928–3937 (2012).
- Smulders, M. M., Schenning, A. P. & Meijer, E. W. Insight into the mechanisms of cooperative self-assembly: the “sergeants-and-soldiers” principle of chiral and achiral C<sub>3</sub>-symmetrical discotic triamides. *J. Am. Chem. Soc.* **130**, 606–611 (2008).
- García, F. et al. The influence of  $\pi$ -conjugated moieties on the thermodynamics of cooperatively self-assembling tricarboxamides. *Chem. Commun.* **49**, 8674–8676 (2013).

- Mohr, S. C., Wilk, W. D. & Barrow, G. M. The association of water with bases and anions in an inert solvent. *J. Am. Chem. Soc.* **87**, 3048–3052 (1965).
- Iwamoto, R. Infrared and near-infrared study of the interaction of amide C=O with water in ideally inert medium. *J. Phys. Chem. A* **114**, 7398–7407 (2010).
- Sorrenti, A., Leira-Iglesias, J., Markvoort, A. J., de Greef, T. F. A. & Hermans, T. M. Non-equilibrium supramolecular polymerization. *Chem. Soc. Rev.* **46**, 5476–5490 (2017).
- Zhao, D. & Moore, J. S. Nucleation-elongation: a mechanism for cooperative supramolecular polymerization. *Org. Biomol. Chem.* **1**, 3471–3491 (2003).
- Venkata Rao, K., Miyajima, D., Nihonyanagi, A. & Aida, T. Thermally bisignate supramolecular polymerization. *Nat. Chem.* **9**, 1133–1139 (2017).
- Gilli, G., Bellucci, F., Ferretti, V. & Bertolasi, V. Evidence for resonance-assisted hydrogen bonding from crystal-structure correlations on the enol form of the  $\beta$ -diketone fragment. *J. Am. Chem. Soc.* **111**, 1023–1028 (1989).
- Filot, I. A. W. et al. Understanding cooperativity in hydrogen-bond-induced supramolecular polymerization: a density functional theory study. *J. Phys. Chem. B* **114**, 13667–13674 (2010).
- Chandler, D. Interfaces and the driving force of hydrophobic assembly. *Nature* **437**, 640–647 (2005).
- Biedermann, F., Nau, W. M. & Schneider, H. J. The hydrophobic effect revisited—studies with supramolecular complexes imply high-energy water as a noncovalent driving force. *Angew. Chem. Int. Ed.* **53**, 11158–11171 (2014).
- Lassette, E. N. The hydrogen bond and association. *Chem. Rev.* **20**, 259–303 (1937).
- Louhichi, A., Jacob, A. R., Bouteiller, L. & Vlassopoulos, D. Humidity affects the viscoelastic properties of supramolecular living polymers. *J. Rheol.* **61**, 1173–1182 (2017).
- Adelizzi, B., Filot, I. A. W., Palmans, A. R. A. & Meijer, E. W. Unravelling the pathway complexity in conformationally flexible *N*-centered triarylamines trisamides. *Chem. Eur. J.* **23**, 6103–6110 (2017).

**Acknowledgements** This project received funding from the European Union’s Horizon 2020 research and innovation program (no. 705701) and the Dutch Ministry of Education, Culture and Science’s Gravitation program (no. 024.001.035). The X-ray diffractometer was financed by the Netherlands Organization for Scientific Research. N.J.V.Z. acknowledges M. L. Ślęczkowski for synthesizing the chiral amine precursor for **1**, B. F. M. de Waal for assistance with Karl Fischer titrations and R. A. A. Bovee for performing MALDI-TOF MS measurements. We also thank S. C. J. Meskers, R. J. M. Nolte and A. J. Markvoort for discussions.

**Reviewer information** Nature thanks C. Hunter, D. Miyajima and D. Pantos for their contribution to the peer review of this work.

**Author contributions** N.J.V.Z. conceived the project and designed the experiments. N.J.V.Z., B.A., X.M., R.H.Z. and A.A. performed the experiments and analysed the data. M.F.J.M. and I.A.W.F. performed the mathematical simulations and density functional theory calculations, respectively. M.L. determined the crystal structure of **2**. N.J.V.Z., M.F.J.M., A.A. and I.A.W.F. wrote the manuscript. A.R.A.P. and E.W.M. supervised the research.

**Competing interests** The authors declare no competing interests.

### Additional information

**Extended data** is available for this paper at <https://doi.org/10.1038/s41586-018-0169-0>.

**Supplementary information** is available for this paper at <https://doi.org/10.1038/s41586-018-0169-0>.

**Reprints and permissions information** is available at <http://www.nature.com/reprints>.

**Correspondence and requests for materials** should be addressed to E.W.M.

**Publisher’s note:** Springer Nature remains neutral with regard to jurisdictional claims in published maps and institutional affiliations.

## METHODS

**Materials.** Solvents used for synthesis were acquired from commercial sources and used as received unless otherwise stated. Spectrophotometric grade methylcyclohexane and heptane were purchased from Sigma Aldrich. [1,1'-Biphenyl]-3,3',5,5'-tetracarboxylic acid was either purchased from TCI Europe (>98%) or prepared as previously reported<sup>31</sup>. Pentafluorophenyl trifluoroacetate (98%), 2-methoxyethylamine (99%) and triethylamine ( $\geq 99\%$ ) were purchased from Sigma Aldrich and used as received. (S)-3,7-Dimethyloctan-1-amine was prepared as previously reported<sup>32</sup> from (S)-citronellol (min. 99%, enantiomeric excess 98.4%) that was purchased from Takasago. Compounds 4,4',4''-nitrioltris(*N*-((S)-3,7-dimethyloctyl)benzamide) (4), 6,6',6''-nitrioltris(*N*-((S)-3,7-dimethyloctyl)nicotinamide) (5) and *N,N',N''*-tris((S)-3,7-dimethyloctyl)benzene-1,3,5-tricarboxamide (6) were prepared as previously reported<sup>29,33</sup>. The photoactivatable dye Cage-552 used for super-resolution fluorescence microscopy was purchased from Abberior.

**Instrumental methods.** Flash column chromatography was performed on a Biotage Isolera One system equipped with an ultraviolet detector. <sup>1</sup>H (400 MHz), <sup>13</sup>C (100 MHz) and <sup>19</sup>F (376 MHz) nuclear magnetic resonance (NMR) spectra were recorded using a Bruker Avance III HD NanoBay spectrometer. <sup>1</sup>H and <sup>13</sup>C NMR spectra were referenced to the residual chloroform signals at 7.26 p.p.m. and 77.23 p.p.m., respectively. NMR spectra are provided in the Supplementary Information. Matrix-assisted laser desorption/ionization time-of-flight mass spectrometry (MALDI-TOF MS) was performed on a Bruker Autoflex Speed spectrometer using  $\alpha$ -cyano-4-hydroxycinnamic acid and 2-[(2*E*)-3-(4-*tert*-butylphenyl)-2-methylprop-2-enylidene]malononitrile as matrices. Infrared spectra were acquired using a Perkin Elmer Spectrum Two spectrometer. Solid samples were analysed using a UATR module. Solutions were analysed using a liquid cell (KBr, *l* = 0.5 mm) and a slide holder module. Baseline spectra of as-received MCH were subtracted from sample spectra. DSC was performed on a TA Instruments Q2000 system. About 5 mg of material was prepared in hermetically sealed aluminium pans and characterized using the following heating program: equilibrate at 35 °C, 35 °C to 300 °C at 10 °C min<sup>-1</sup>, 300 °C to -50 °C at -10 °C min<sup>-1</sup>, -50 °C to 300 °C at 10 °C min<sup>-1</sup>. Micro-DSC was performed on a TA Instruments Multicell DSC. About 1.0 ml of material was prepared in Hastelloy ampoules and characterized using the following heating program: equilibrate at 25 °C, 25 °C to 60 °C at 60 °C h<sup>-1</sup>, equilibrate for 15 min, 60 °C to 0 °C at 60 °C h<sup>-1</sup>, equilibrate for 15 min, 0 °C to 60 °C at 60 °C h<sup>-1</sup>, equilibrate for 15 min, 60 °C to 0 °C at 60 °C h<sup>-1</sup>, equilibrate for 15 min, 0 °C to 60 °C at 60 °C h<sup>-1</sup>, equilibrate for 15 min, 60 °C to 0 °C at 30 °C h<sup>-1</sup>, equilibrate for 15 min, 0 °C to 60 °C at 30 °C h<sup>-1</sup>, equilibrate for 15 min, 60 °C to 0 °C at 15 °C h<sup>-1</sup>, equilibrate for 15 min, 0 °C to 60 °C at 15 °C h<sup>-1</sup>, 60 °C to 25 °C at 60 °C h<sup>-1</sup>. Baseline curves of as-received MCH were subtracted from sample curves. Polarized optical microscopy was performed on a Leica CTR 6000 microscope equipped with two crossed polarizers, a Linkam hot-stage THMS600 as the sample holder, a Linkam TMS94 controller and a Leica DFC420 C camera. Ultraviolet, CD and linear dichroism spectroscopies were performed using a Jasco J-815 spectrometer equipped with a Jasco PTC-348WI Peltier-type temperature controller. The sample holder was purged with nitrogen at a flow rate of 20 l min<sup>-1</sup>. Quartz cuvettes (Hellma Analytics) with path lengths of 10 mm, 5 mm and 1 mm were used. The cuvette with a path length of 10 mm was equipped with a screw cap that was fitted with a Teflon-lined septum, and those with 5- and 1-mm path lengths were sealed with a Teflon stopper. Before all cooling and heating traces were acquired, samples were equilibrated at 95 °C for 15 min. All measurements were conducted using the sealable 10-mm cuvette unless specifically stated. All variable temperature measurements were performed using a cooling rate of 60 °C h<sup>-1</sup> unless otherwise stated. Karl Fischer titrations were performed using a Mettler-Toledo C30 Coulometric KF Titrator loaded with CombiCoulomat Frit KF reagent (for cells with diaphragm, contains methanol, purchased from Merck). Approximately 1 g of sample was used for a typical single Karl Fischer titration. In a modification of a previously reported procedure<sup>34</sup>, light-scattering measurements were performed using a Malvern  $\mu$ V Zetasizer equipped with an 830-nm laser and a scattering angle of 90°. Samples were prepared with as-received MCH that had been filtered through a 0.45  $\mu$ m Whatman Anaport 10 syringe filter. Measurements were acquired after equilibrating for 10 min at the desired temperature. Samples for wide-angle X-ray scattering were mounted on V1 grade mica sheets with a thickness of 5–7  $\mu$ m and measured for 15-min exposures using a SAXSLAB GANESHA system equipped with a GeniX-Cu ultralow divergence source producing X-ray photons with a wavelength of 1.54 Å and a flux of  $1 \times 10^8$  photons per second. Scattering patterns were collected using a Pilatus 300K silicon pixel detector, and the beam centre and the *q* range were calibrated using the diffraction peaks of silver behenate. Conversion of two-dimensional images into one-dimensional spectra was accomplished with SaxsGui software. Domain spacings were calculated using primary scattering peak positions (*q*<sup>\*</sup>) and interplanar spacings (*d*<sup>\*</sup> =  $2\pi/q^*$ ). For columnar hexagonal morphologies, the centre-to-centre distance was calculated as  $2d^*/\sqrt{3}$ . AFM was performed using an Asylum Research MFP-3D system in non-contact tapping mode. Images were processed using Gwyddion 2.49.

**Synthesis.** Tetrakis(perfluorophenyl)[1,1'-biphenyl]-3,3',5,5'-tetracarboxylate (7). [1,1'-Biphenyl]-3,3',5,5'-tetracarboxylic acid (1.0 g, 3.0 mmol, 1.0 equiv.) was suspended in 50 ml of acetonitrile in a 250-ml flask equipped with a magnetic stir bar. Triethylamine (3.1 ml, 24 mmol, 8.0 equiv.) was added, and the mixture became homogeneous after stirring for approximately 10 min. A solution of pentafluorophenyl trifluoroacetate (3.1 ml, 19 mmol, 6.0 equiv.) in acetonitrile (2 ml) was then added dropwise. After the addition was complete, the headspace was purged with argon and the mixture was stirred at room temperature. After 5 h, the mixture was cooled with an ice bath. The solids were collected on a fine sintered glass frit and washed with cold acetonitrile. After drying in a vacuum oven at 50 °C, 7 (3.0 g, 98%) was isolated as a bright white powder that was sufficiently pure for use in subsequent reactions without further purification. <sup>1</sup>H NMR (400 MHz, CDCl<sub>3</sub>):  $\delta$  9.11 (t, 2H), 8.81 (d, 4H). <sup>19</sup>F NMR (376 MHz, CDCl<sub>3</sub>):  $\delta$  -152.14 (m, 8F), -156.49 (m, 4F), -161.45 (m, 8F).

*N*<sup>3</sup>,*N*<sup>3'</sup>,*N*<sup>5</sup>,*N*<sup>5'</sup>-tetrakis((S)-3,7-dimethyloctyl)-[1,1'-biphenyl]-3,3',5,5'-tetracarboxamide (1). Compound 7 (0.32 g, 0.32 mmol, 1.0 equiv.) was dissolved in 10 ml dry THF in a 50-ml flask equipped with a magnetic stir bar. (S)-3,7-Dimethyloctan-1-amine (0.41 g, 2.6 mmol, 8.0 equiv.) and triethylamine (0.36 ml, 2.6 mmol, 8.0 equiv.) were diluted with 3 ml dry THF and added dropwise to the solution of 7 at room temperature. The headspace was purged with argon, and the mixture was stirred for 16 h at 50 °C. After cooling to room temperature, the solvent was removed by rotary evaporation and the crude solid was dissolved in chloroform. This solution was washed with 1 M NaOH, 1 M HCl and brine. The organic phase was dried with MgSO<sub>4</sub> and filtered. The solvent was removed by rotary evaporation, and the resulting solid was purified by flash column chromatography (eluent, 15% ethyl acetate in chloroform). 1 was isolated as a white waxy solid (0.20 g, 70%) after removing the solvent by rotary evaporation and subsequently drying under vacuum (<100 mTorr) in a desiccator with P<sub>2</sub>O<sub>5</sub>. The material was stored in a desiccator loaded with CaSO<sub>4</sub>. <sup>1</sup>H NMR (400 MHz, CDCl<sub>3</sub>):  $\delta$  8.02 (m, 2H), 7.90 (m, 4H), 6.76 (broad t, 6.76), 3.50 (m, 8H), 1.08–1.74 (m, 40H), 0.96 (d, 12H), 0.86 (d, 24). <sup>13</sup>C NMR (100 MHz, CDCl<sub>3</sub>):  $\delta$  166.72, 140.13, 136.02, 128.26, 125.02, 39.49, 38.89, 37.41, 36.93, 31.14, 28.18, 24.90, 22.93, 22.83, 19.76. MALDI-TOF MS: calculated *m/z* for C<sub>56</sub>H<sub>94</sub>N<sub>4</sub>O<sub>4</sub>: 886.73, found: 887.77 ([M + H]<sup>+</sup>), 909.76 ([M + Na]<sup>+</sup>).

*N*<sup>3</sup>,*N*<sup>3'</sup>,*N*<sup>5</sup>,*N*<sup>5'</sup>-tetrakis(2-methoxyethyl)-[1,1'-biphenyl]-3,3',5,5'-tetracarboxamide (2). Compound 7 (0.40 g, 0.40 mmol, 1.0 equiv.) was dissolved in 10 ml dry THF in a 50-ml flask equipped with a magnetic stir bar. 2-Methoxyethylamine (0.24 g, 3.2 mmol, 8.0 equiv.) and triethylamine (0.45 ml, 3.2 mmol, 8.0 equiv.) were diluted with 3 ml dry THF and added dropwise to the solution of 7 at room temperature. The headspace was purged with argon, and the mixture was stirred for 16 h at 50 °C. After cooling to room temperature, the solvent was removed by rotary evaporation, and the crude solid was dissolved in chloroform. This solution was washed with 1 M NaOH, 1 M HCl and brine. The organic phase was dried with MgSO<sub>4</sub> and filtered. The crude 2 was serially recrystallized by dissolving in chloroform with methanol and layering with pentane to yield approximately 50 mg (22%) of colourless needles. Crystals suitable for X-ray diffraction were formed by vapour diffusion of pentane into a solution of chloroform and methanol. <sup>1</sup>H NMR (400 MHz, CDCl<sub>3</sub>):  $\delta$  8.05 (m, 2H), 7.83 (m, 4H), 7.52 (t, 4H), 3.62–3.72 (m, 16H), 3.39 (s, 12H). <sup>13</sup>C NMR (100 MHz, CDCl<sub>3</sub>):  $\delta$  166.66, 140.09, 135.44, 128.35, 125.12, 71.19, 58.86, 40.27. MALDI-TOF MS: calculated *m/z* for C<sub>28</sub>H<sub>38</sub>N<sub>4</sub>O<sub>8</sub>: 558.27, found: 559.30 ([M + H]<sup>+</sup>), 581.28 ([M + Na]<sup>+</sup>), 597.25 ([M + K]<sup>+</sup>).

**Preparation of samples with variable water content.** The water content of MCH is highly dependent on the relative humidity of the atmosphere if handled without special precautions. Care must be taken to ensure that samples are completely sealed during spectroscopic measurements that take place in an inert atmosphere. Cuvettes equipped with a screw cap and a Teflon-lined septum were found to be best suited for these measurements. To determine the water content after analysis by CD spectroscopy, dilute samples were directly injected into the Karl Fischer titration instrument after withdrawing from the sealed cuvette by syringe. All Karl Fischer titration measurements were performed in duplicate and expressed as mean  $\pm$  s.d. unless otherwise stated.

At the ambient humidity in the laboratory in which this research was carried out, as-received MCH contained  $32 \pm 3$  p.p.m. H<sub>2</sub>O (mean  $\pm$  s.d. of four measurements). MCH was dried by sparging with argon and then storing over activated 3 Å molecular sieves overnight in a sealed bottle. After bringing into a nitrogen-filled glovebox, the MCH was passed through a 0.2- $\mu$ m Whatman Anaport 10 syringe filter. The typical water content for dry MCH prepared in this way was  $<0.1$  p.p.m. (that is, below the level of detection of the Karl Fischer titration). Dry samples were prepared in a nitrogen-filled glovebox with dry MCH, taking special care to use oven-dried glassware and Teflon-lined caps for vials. Alternatively, in a modification of a previously reported procedure<sup>35</sup>, dry samples may be prepared with as-received MCH in sealable cuvettes by exposure to a nitrogen-purged atmosphere (for example, in the sample holder of a CD spectrometer) for a short time at 20 °C before starting the measurement.

Wet MCH was prepared by layering MCH (around 20 ml) over water (around 1 ml) that was purified with an EMD Milipore Mili-Q Integral Water Purification System. After allowing to set for at least 2 h, wet MCH was carefully withdrawn with a syringe from the top layer without disturbing the bottom water phase. Wet samples were prepared on the benchtop; care must be taken to minimize exposure of the solvent to the atmosphere by quickly sealing the sample vials. Wet MCH transferred in this way contained approximately 60 p.p.m. water. To form **C** at 20 °C in MCH (for example, in preparation for characterization by infrared spectroscopy), a small drop of water may be added to a sample of **A** or **B** that has been prepared using dry or as-received MCH, respectively. Gentle agitation to facilitate mixing (that is, inversion of the vial) resulted in the formation of **C** within seconds.

To prepare wet samples for AFM analysis, solutions of **6** were prepared in wet MCH and then drop-cast onto mica. The sample was left to evaporate in a Petri dish that contained 1 ml of water. The dish was covered and allowed to stand overnight at room temperature before imaging. The sample was not allowed to come into direct contact with the water droplet. To prepare dry samples for AFM analysis, solutions of **6** were prepared in dry MCH and then drop-cast onto mica in the glovebox. The dish was covered and allowed to stand overnight in the glovebox at room temperature before imaging.

**Bulk characterization of 1.** Using DSC, phase-transition temperatures and their corresponding enthalpies were determined from the cooling and second heating traces with cooling and heating rates of 10 °C min<sup>-1</sup> (Extended Data Fig. 1a). The isotropic melt was reached at 273 °C, and another phase transition was observed at 262 °C; the total enthalpy of these two transitions is 38 J g<sup>-1</sup>. The corresponding exothermic transitions were observed in the cooling trace at 269 °C and 259 °C, respectively. No additional phase transitions were observed between 259 °C and -50 °C. Using polarized optical microscopy, mosaic and focal conic textures were observed, similar to those reported for benzene tricarboxamide-based liquid crystals<sup>36</sup>. Extended Data Fig. 1b shows this texture at 135 °C after cooling from the isotropic melt at 10 °C min<sup>-1</sup>. The liquid crystalline structure of **1** was characterized by wide-angle X-ray scattering. The scattering pattern as well as the lattice parameters of **1** at 20 °C are shown in Extended Data Fig. 1c. In the small angle regime, three reflections were observed with  $q$  values of 3.0, 5.2 and 6.0 nm<sup>-1</sup>. The reciprocal spacing ratio is calculated as 1:√3:2, which is assigned to the columnar hexagonal liquid crystal structure with the corresponding lattice distances  $d[100] = 2.1$  nm,  $d[110] = 1.2$  nm and  $d[200] = 1.1$  nm, respectively. From  $d[100]$ , the domain spacing,  $L_0$ , is 24 Å. In the wide-angle regime, the reflection at 19.8 nm<sup>-1</sup> gives a  $d$ -spacing of 3.2 Å, which we assign to the interdiscotic distance. These dimensions are similar to those observed for benzene tricarboxamide-based aggregates<sup>16</sup>.

Bulk **1** was further characterized by CD and FTIR spectroscopies. Bulk **1** was prepared for analysis by CD spectroscopy by drop-casting a 2.0 mM solution of **1** in MCH onto a quartz slide. After most of the MCH had evaporated in the ambient atmosphere, the film was heated to 100 °C using the Peltier controller of the CD spectrometer for 1 h. The resulting spectrum (Extended Data Fig. 1d) shows a positive Cotton effect at 255 nm. The full FTIR spectrum of bulk **1** cooled from isotropic melt is presented in Extended Data Fig. 1e, and the comparison of the N–H stretching and the amide I and amide II bands of bulk **1** and **A** ([**1**] = 2.0 mM in dry MCH) are shown in Extended Data Fig. 1f.

**van 't Hoff analyses.** The enthalpy of elongation,  $\Delta H_e$ , for the formation of **A** was estimated from a van 't Hoff plot of  $\ln(K_e)$  versus  $1/T_e$  (Extended Data Fig. 4a;  $K_e = a_1^{-1}$ ,  $a_1 = [1]/[1]_{\text{ref}}$ ,  $[1]_{\text{ref}} = 1 \mu\text{M}$  in MCH and  $T_e$  is the elongation temperature at a given [**1**]). The elongation temperatures were identified using scripts written previously<sup>37</sup>. This procedure has been previously used to estimate the  $\Delta H_e$  for other cooperative supramolecular polymerizations<sup>17</sup>. For **A** → **B** and **B** → **C**, an analogous procedure was used to estimate the corresponding molar enthalpies of hydration for each process,  $\Delta H_{\text{hyd,A}}$  and  $\Delta H_{\text{hyd,B}}$ , respectively (Extended Data Fig. 4b, c). We assumed that **A** and **B** are in equilibrium with molecularly dissolved water in each respective transition. For each transition,  $\ln(K_{\text{hyd,A}})$  and  $\ln(K_{\text{hyd,B}})$  ( $K_{\text{hyd}} = a_{\text{H}_2\text{O}}^{-1}$ ,  $a_{\text{H}_2\text{O}} = [\text{H}_2\text{O}]/[\text{H}_2\text{O}]_{\text{ref}}$  and  $[\text{H}_2\text{O}]_{\text{ref}} = 1 \mu\text{M}$  in MCH) were plotted against  $1/T_{\text{A} \rightarrow \text{B}}$  and  $1/T_{\text{B} \rightarrow \text{C}}$ , respectively. The critical temperatures  $T_{\text{A} \rightarrow \text{B}}$  and  $T_{\text{B} \rightarrow \text{C}}$  were identified using the second derivative of each corresponding VT-CD curve (Extended Data Fig. 4d). On the basis of the independence of **A** → **B** and **B** → **C** to the concentration of **1** (Fig. 1e), we assumed that the activities of **A**, **B** and **C** were constants.

**Super-resolution microscopy.** A modification of previously reported PALM<sup>38</sup> and iPAINT<sup>39</sup> protocols were used to visualize fibres of **1** and **6**. A detailed description of this technique is in preparation and will be published elsewhere. In short, 200 μM solutions of each aggregate were stained with 1% v/v of Cage-552 (10 mM in DMSO) and 1% v/v of *i*-PrOH. Each prepared sample was injected into a sample chamber constructed from a glass cover slide and coverslip held together with double-sided tape, and iPAINT images were acquired using a Nikon N-STORM system as described previously<sup>39</sup>. Time-lapses of  $15 \times 10^3$  frames were recorded onto a  $256 \times 256$  pixel region (pixel size 170 nm) of an EMCCD camera (ixon3, Andor) at a rate of 47 frames per second. To perform single-molecule experiments, a low

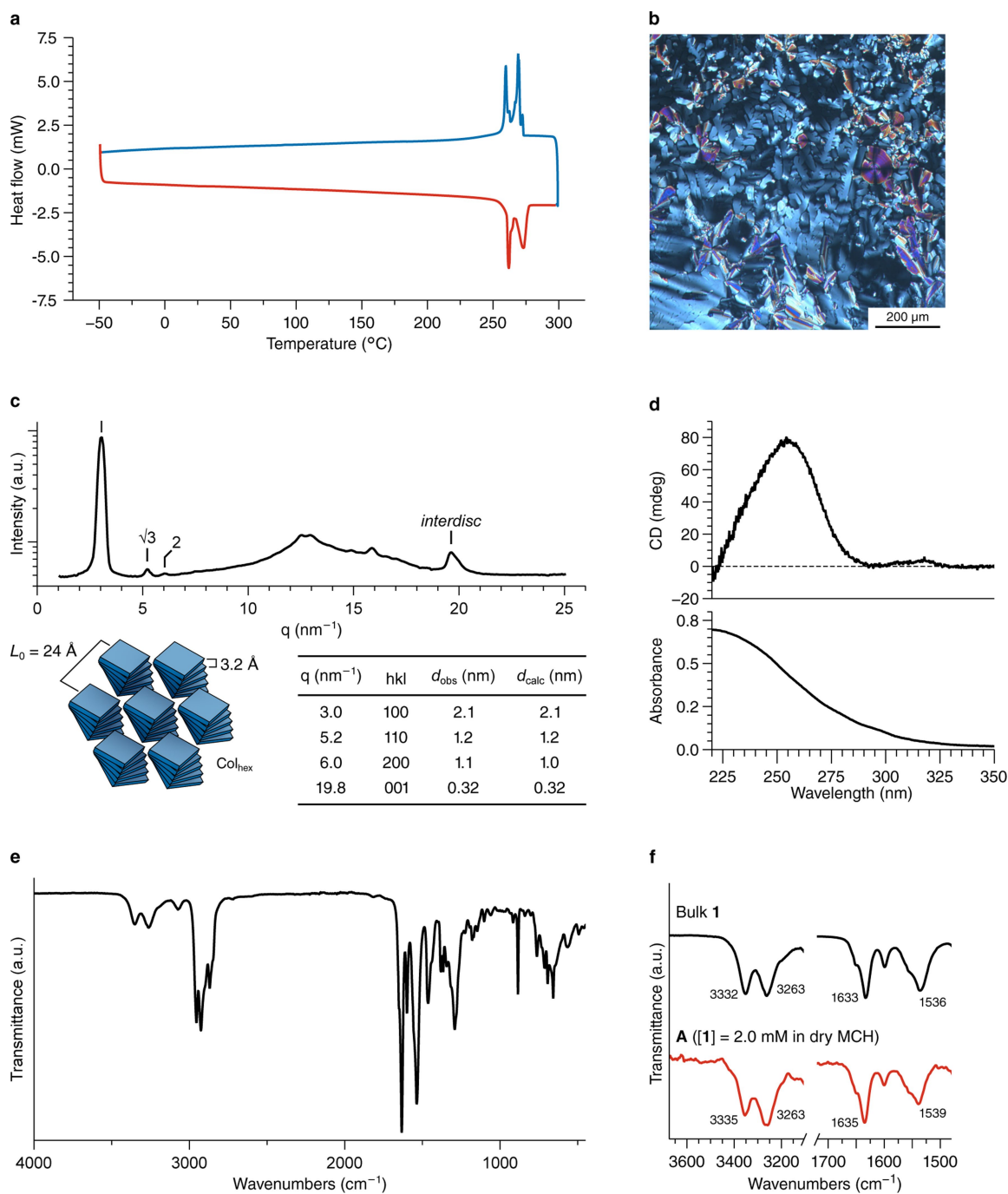
ultraviolet laser light power (1.6 mW cm<sup>-2</sup> power at 405 nm) is used to uncage a small amount of dye per frame, statistically ensuring a spatial separation greater than the diffraction limit of light. The sample is subsequently irradiated at 561 nm with a laser of optical intensity 488 mW cm<sup>-2</sup> to excite the single molecules that were previously photoactivated. The high-power laser bleaches the excited molecules, so that a new subset of molecules can be photoactivated, excited and localized. The localization of single molecules is finally carried out by NIS-element Nikon software. The procedure for the thickness analyses is detailed in the Supplementary Information.

**X-ray crystal structure determination of 2.** C<sub>28</sub>H<sub>38</sub>N<sub>4</sub>O<sub>8</sub>·2CHCl<sub>3</sub>,  $M_w = 797.36$  g mol<sup>-1</sup>, colourless needle,  $0.53 \times 0.14 \times 0.02$  mm<sup>3</sup>, triclinic,  $P\bar{1}$  (no. 2),  $a = 12.2183(9)$ ,  $b = 14.9730(9)$ ,  $c = 16.0255(9)$  Å,  $\alpha = 73.220(3)$ ,  $\beta = 82.014(2)$ ,  $\gamma = 77.416(3)^\circ$ ,  $V = 2,730.4(3)$  Å<sup>3</sup>,  $Z = 3$ ,  $D_x = 1.455$  g cm<sup>-3</sup>,  $\mu = 0.53$  mm<sup>-1</sup>. 70,947 reflections were measured on a Bruker Kappa ApexII diffractometer with sealed tube and Triumph monochromator ( $\lambda = 0.71073$  Å) at a temperature of 150(2) K up to a resolution of  $(\sin \theta/\lambda)_{\text{max}} = 0.65$  Å<sup>-1</sup>. The intensities were integrated with the Eval15 software<sup>40</sup>. Numerical absorption correction and scaling was performed with SADABS<sup>41</sup> (correction range 0.73–1.00). 12,556 reflections were unique ( $R_{\text{int}} = 0.062$ ), of which 7,428 were observed ( $I > 2\sigma(I)$ ). The structure was solved with Patterson superposition methods using SHELXT<sup>42</sup>. Least-squares refinement was performed with SHELXL-2016<sup>43</sup> against  $F^2$  of all reflections. Non-hydrogen atoms were refined freely with anisotropic displacement parameters. One of the chloroform molecules was refined with a disorder model. Hydrogen atoms were introduced in calculated positions. N–H hydrogen atoms were refined freely with isotropic displacement parameters. C–H hydrogen atoms were refined with a riding model. 707 parameters were refined with 168 restraints (distances, angles and displacement parameters of the chloroform molecules).  $R1/wR2$  ( $I > 2\sigma(I)$ ): 0.0619/0.1528.  $R1/wR2$  (all reflections): 0.1189/0.1826.  $S = 1.029$ . Residual electron density between -0.74 and 1.10 e Å<sup>-3</sup>. Geometry calculations and checking for higher symmetry were performed with the PLATON program<sup>44</sup>.

**Computational settings.** Density functional theory simulations were performed using VASP. The PBE exchange-correlation functional was used in conjunction with the projector augmented wave approach. All structures were optimized to their local minima using the conjugate gradient algorithm as implemented in VASP. The nature of the stationary points was evaluated from the harmonic modes, computed numerically by using a complete Hessian matrix (that is, incorporating all degrees of freedom). No imaginary frequencies were found for the optimized structures with the exception of some degrees of freedom corresponding to rotation and translation, which confirms that these geometries correspond to local minima on the potential energy surface. Optimization and other electronic settings are provided in the Supplementary Information.

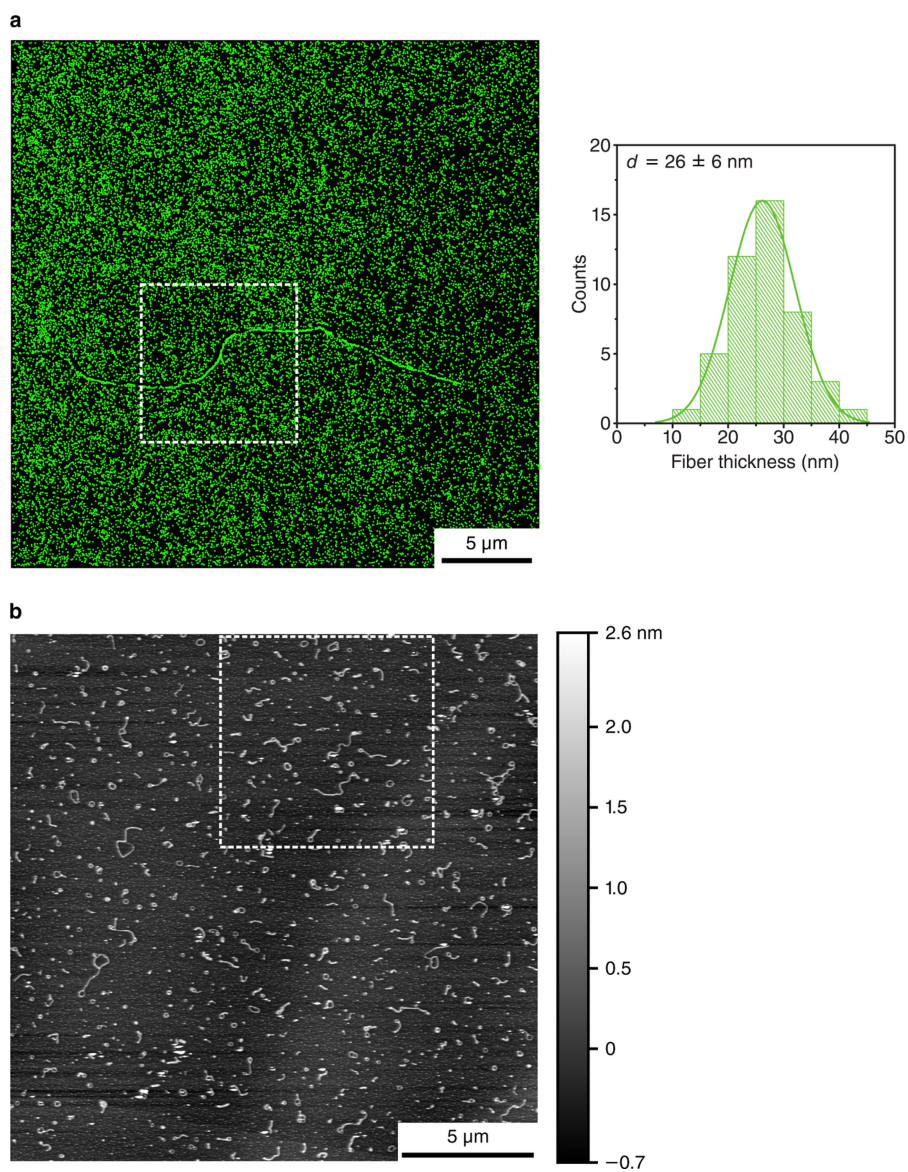
**Data availability.** Data that support the findings of this study are available within the paper and its Supplementary Information. Metrical parameters for **2** are available free of charge from the Cambridge Crystallographic Data Centre (<https://www.ccdc.cam.ac.uk>) under reference number CCDC 1562237.

- Mazik, M. & König, A. Recognition properties of an acyclic biphenyl-based receptor toward carbohydrates. *J. Org. Chem.* **71**, 7854–7857 (2006).
- Suthagar, K., Watson, A. J., Wilkinson, B. L. & Fairbanks, A. J. Synthesis of arabinose glycosyl sulfamides as potential inhibitors of mycobacterial cell wall biosynthesis. *Eur. J. Med. Chem.* **102**, 153–166 (2015).
- Brunsveld, L. et al. Chiral amplification in columns of self-assembled *N,N,N'*-tris((S)-3,7-dimethyloctyl)benzene-1,3,5-tricarboxamide in dilute solution. *Chem. Lett.* **29**, 292–293 (2000).
- Boekhoven, J. et al. Dissipative self-assembly of a molecular gelator by using a chemical fuel. *Angew. Chem. Int. Ed.* **49**, 4825–4828 (2010).
- Christian, S. D., Afsprung, H. E., Johnson, J. R. & Worley, J. D. Control and measurement of water activity. *J. Chem. Educ.* **40**, 419–421 (1963).
- van Gorp, J. J., Vekemans, J. A. J. M. & Meijer, E. W. C<sub>3</sub>-symmetrical supramolecular architectures: fibers and organic gels from discotic trisamides and trisureas. *J. Am. Chem. Soc.* **124**, 14759–14769 (2002).
- Markvoort, A. J., ten Eikelder, H. M., Hilbers, P. A., de Greef, T. F. & Meijer, E. W. Theoretical models of nonlinear effects in two-component cooperative supramolecular copolymerizations. *Nat. Commun.* **2**, 509 (2011).
- Aloi, A. et al. Imaging nanostructures by single-molecule localization microscopy in organic solvents. *J. Am. Chem. Soc.* **138**, 2953–2956 (2016).
- Aloi, A., Vilanova, N., Albertazzi, L. & Voets, I. K. iPAINT: a general approach tailored to image the topology of interfaces with nanometer resolution. *Nanoscale* **8**, 8712–8716 (2016).
- Schreurs, A. M. M., Xian, X. & Kroon-Batenburg, L. M. J. EVAL15: a diffraction data integration method based on ab initio predicted profiles. *J. Appl. Crystallogr.* **43**, 70–82 (2010).
- Sheldrick, G. M. SADABS (Univ. Göttingen, 2008).
- Sheldrick, G. M. SHELXT - integrated space-group and crystal-structure determination. *Acta Crystallogr. A* **71**, 3–8 (2015).
- Sheldrick, G. M. Crystal structure refinement with SHELXL. *Acta Crystallogr. C* **71**, 3–8 (2015).
- Spek, A. L. Structure validation in chemical crystallography. *Acta Crystallogr. D* **65**, 148–155 (2009).



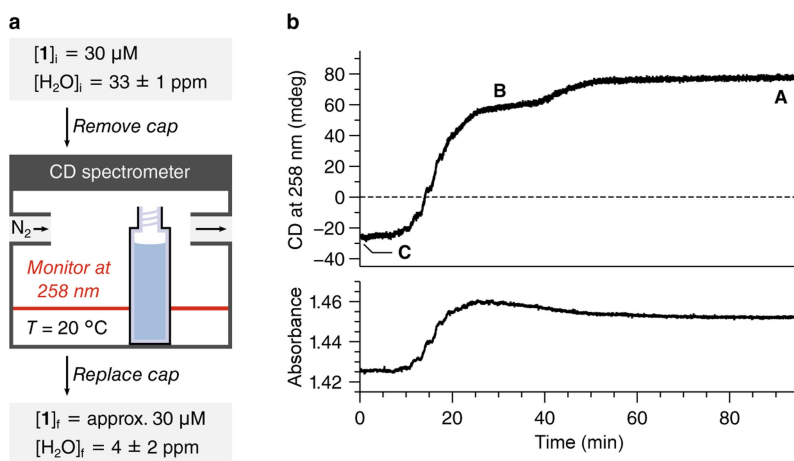
**Extended Data Fig. 1 | Bulk characterization of 1.** **a**, DSC trace of **1** (cooling in blue, second heating in red). **b**, Polarized optical microscopy image of **1** with crossed polarizers at 135 °C after cooling from the isotropic melt. **c**, Wide-angle X-ray scattering trace of bulk **1** at room temperature (top) with a schematic of the hexagonal columnar

morphology (bottom left) and tabulated parameters (bottom right). **d**, CD signal (top) and absorbance (bottom) of a thin film of **1** at 20 °C. **e**, FTIR spectrum of bulk **1** at 20 °C after cooling from the isotropic melt. **f**, Comparison of the FTIR spectra of bulk **1** after cooling from the isotropic melt and **A** ( $[1] = 2.0$  mM in dry MCH, labels in  $\text{cm}^{-1}$ ).



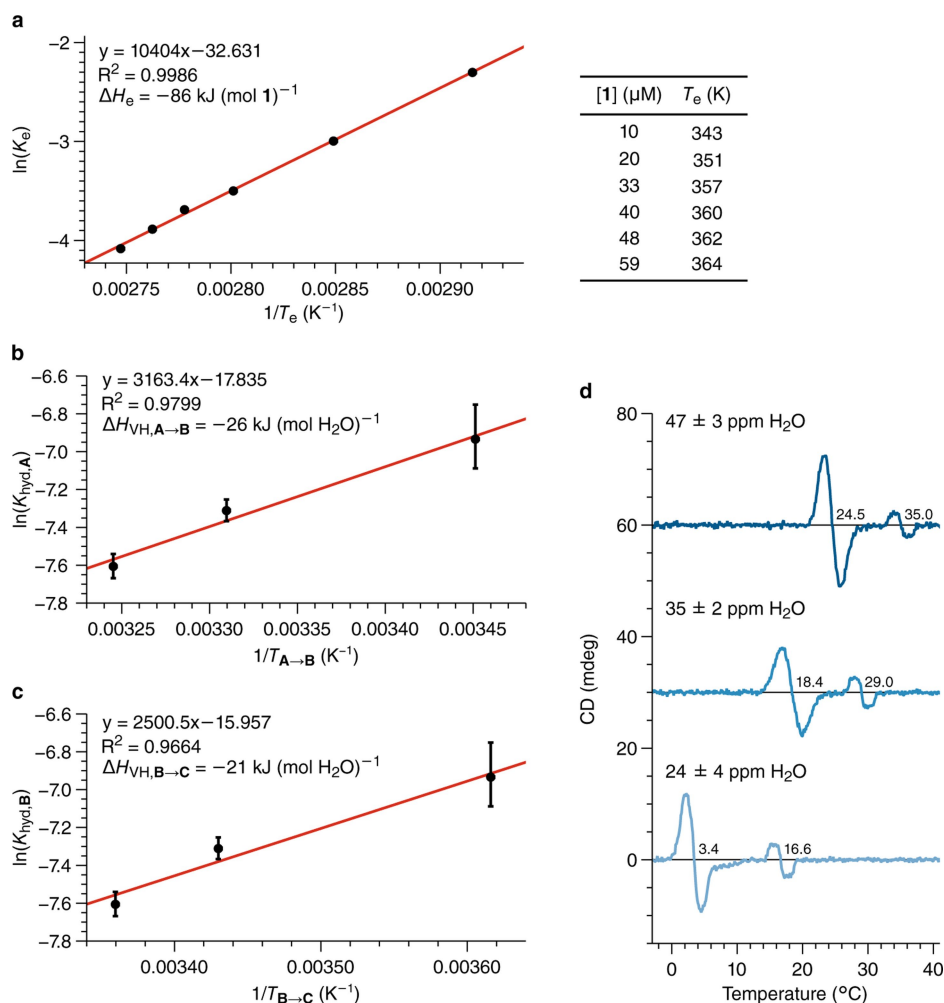
**Extended Data Fig. 2 | Super-resolution fluorescence and AFM images of 1.** **a**, Supramolecular fibres of **1** stained with Cage-552 photoactivatable dye imaged by super-resolution fluorescence microscopy (left) and corresponding thickness analysis (right). The indicated zone in the

microscopy image is depicted in Fig. 1b. A discussion of the thickness analysis and a comparison to fibres of **6** is provided in the Supplementary Information. **b**, Supramolecular fibres of **1** imaged by AFM in non-contact tapping mode. The indicated zone is depicted in Fig. 1c.



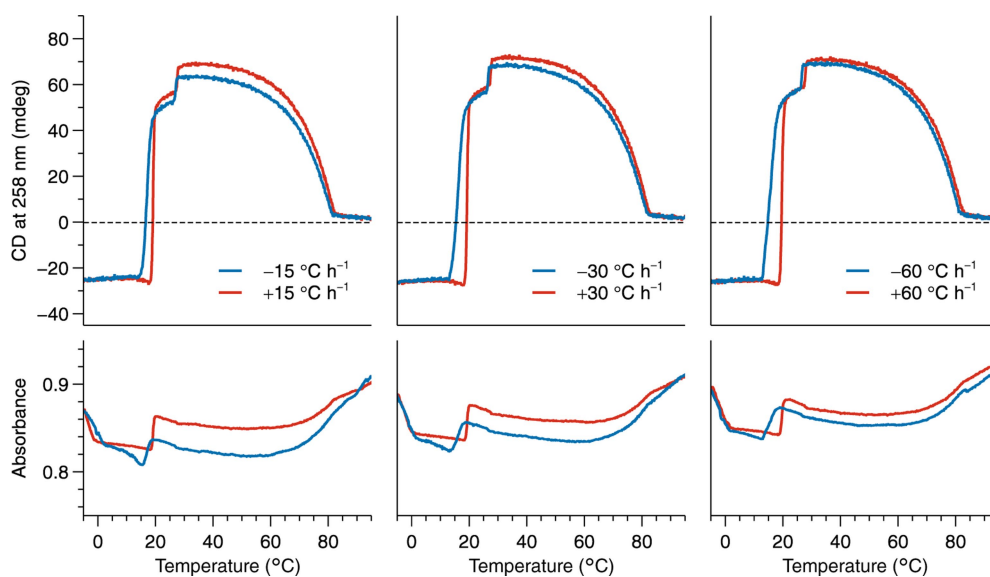
**Extended Data Fig. 3 | Removal of water from aggregates of 1 to effect helicity transitions.** **a**, Schematic of experimental design. The CD spectrometer was purged with nitrogen at a rate of  $20 \text{ l min}^{-1}$ . **b**, CD

signal (top) and absorbance (bottom) at 258 nm as a  $30 \mu\text{M}$  solution of **1** is dried over 100 min in the sample holder of the CD spectrometer. All water content measurements are reported as mean  $\pm$  s.d. ( $n = 2$ ).



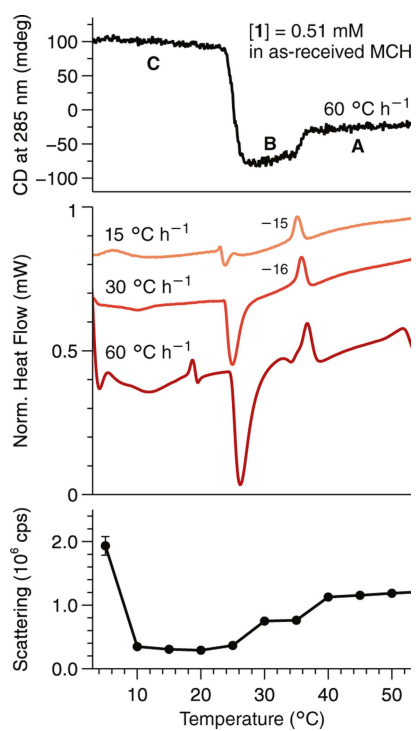
**Extended Data Fig. 4 | van 't Hoff analyses.** **a**, van 't Hoff plot of  $\ln(K_c)$  versus  $1/T_e$  (left) with tabulated  $T_e$  data (right). **b**, van 't Hoff plot of  $\ln(K_{\text{hyd},A})$  versus  $1/T_{A \rightarrow B}$ . The points represent  $\ln(K_{\text{hyd},A})$  calculated using the mean of the water content determined for each respective measurement. The error bars correspond to the spread of  $\ln(K_{\text{hyd},A})$  as a result of the experimental uncertainty of each respective water content measurement. **c**, van 't Hoff plot of  $\ln(K_{\text{hyd},B})$  versus  $1/T_{B \rightarrow C}$ . The points

represent  $\ln(K_{\text{hyd},B})$  calculated using the mean of the water content determined for each respective measurement. The error bars correspond to the spread of  $\ln(K_{\text{hyd},B})$  as a result of the experimental uncertainty of each respective water content measurement. **d**, Determination of  $T_{A \rightarrow B}$  and  $T_{B \rightarrow C}$  from the second derivative of the corresponding VT-CD curves presented in Fig. 1f (labels in  $^{\circ}\text{C}$ ).

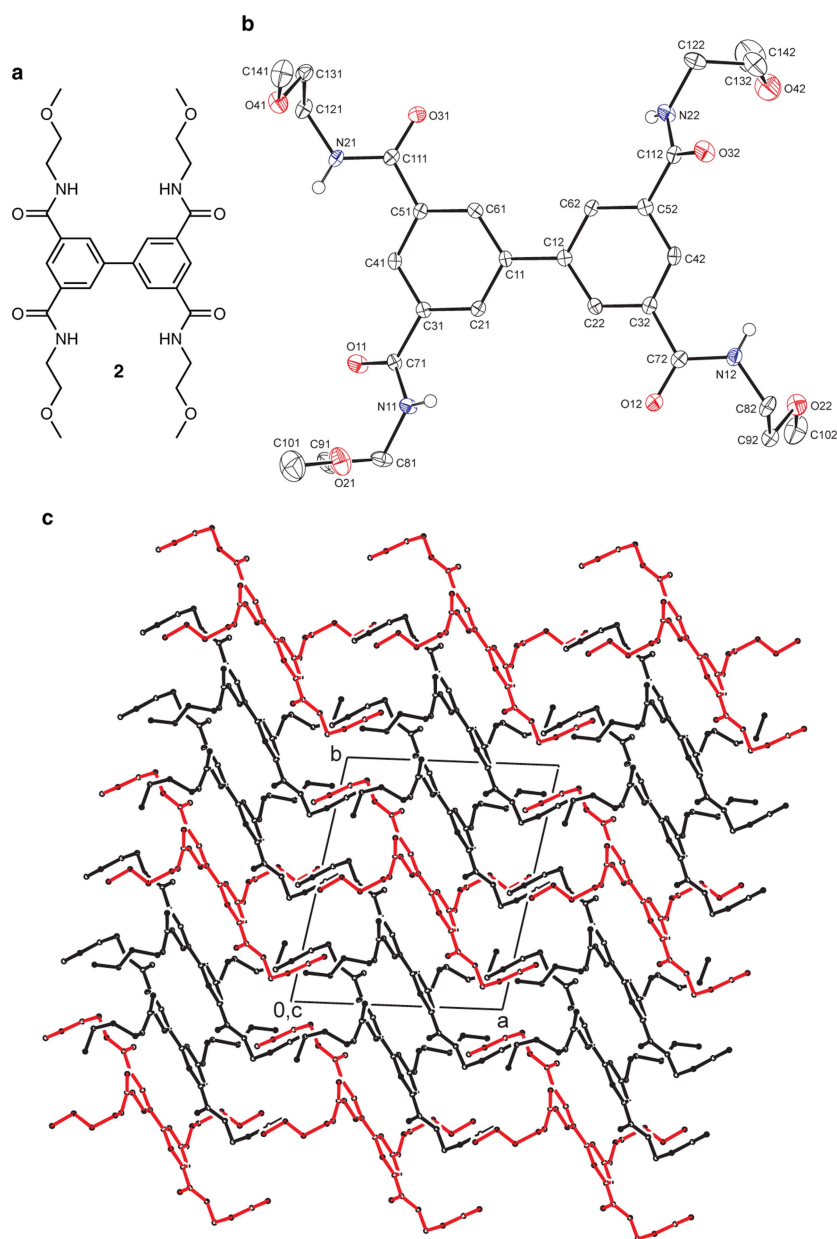


**Extended Data Fig. 5 | Cooling and heating experiments using VT-CD spectroscopy.** The CD intensity was monitored at 258 nm while cooling from 95 °C to -5 °C and then immediately heating back to 95 °C with

scanning rates of 15 (left), 30 (middle) and 60 °C h<sup>-1</sup> (right). Samples were prepared with as-received MCH ([1] = 30 μM, [H<sub>2</sub>O] = 35 ± 2 p.p.m.).

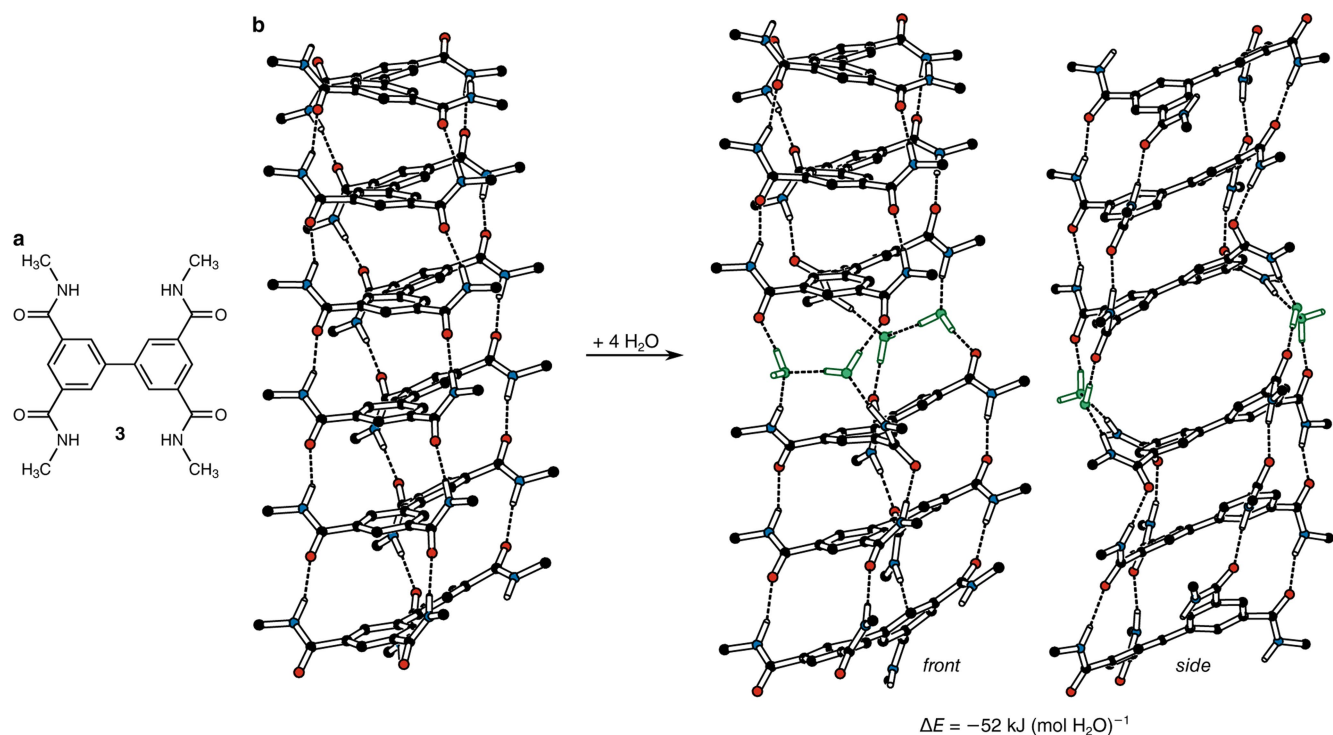
**Extended Data Fig. 6 | Heating experiments with aggregates of 1.**

A 0.51  $\mu\text{M}$  solution of **1** in as-received MCH was characterized by VT-CD spectroscopy (top), micro-DSC (middle) and light scattering (bottom, mean  $\pm$  s.d. ( $n = 5$ ) are shown). In the micro-DSC plot, only the endothermic transitions corresponding to **B**  $\rightarrow$  **A** with scan rates of 15 and 30  $^{\circ}\text{C h}^{-1}$  had baselines suitable for integration (labels in  $\text{kJ (mol 1)}^{-1}$ ).



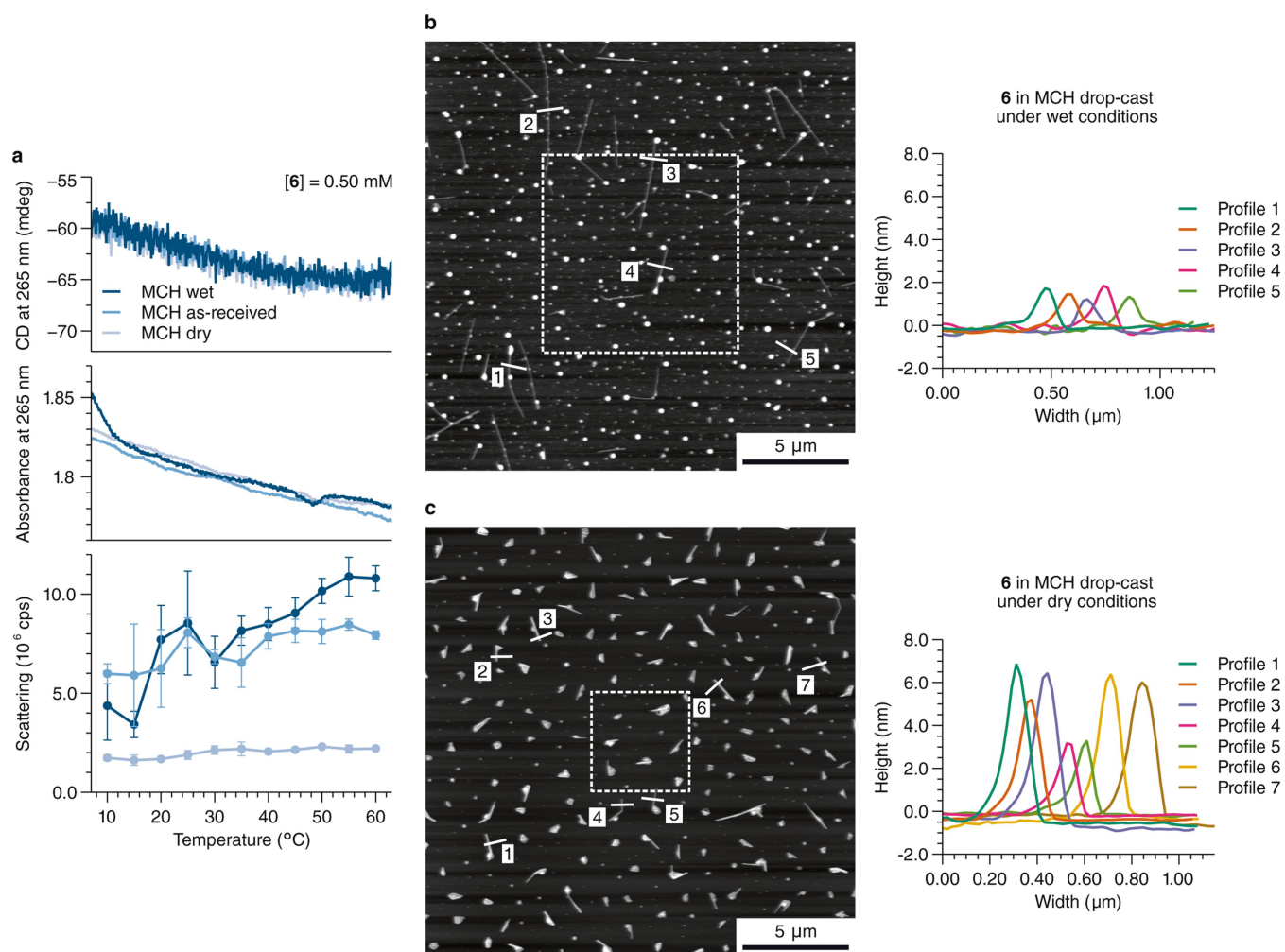
**Extended Data Fig. 7 | Crystal structure of 2.** **a**, Chemical structure of 2. **b**, Displacement ellipsoid plot (50% probability level) of 2 in the crystal. C–H hydrogen atoms and chloroform solvent molecules are omitted for clarity. Only one of two independent molecules is shown. The other independent molecule is located on an inversion centre. **c**, Packing of 2

in the crystal. The two independent molecules are shown in black and red, respectively. Hydrogen atoms and chloroform solvent molecules are omitted for clarity. The structure shows pseudo-translational symmetry in the *b*-direction.



**Extended Data Fig. 8 | Molecular model of water binding to an aggregate of biphenyl tetracarboxamide molecules.** **a**, Chemical structure of **3**. **b**, Molecular models based on density functional theory calculations for the incorporation of four water molecules into a

hexameric aggregate of **3**. Hydrogen atoms, apart from those engaged in hydrogen bonding, are omitted for clarity. The structures are colour coded as follows: hydrogen bond, dashed lines; carbon, black; oxygen, red; nitrogen, blue; water molecules, green.



**Extended Data Fig. 9 | The influence of water content on the self-assembly of 6 in MCH.** **a**, CD signal (top), ultraviolet absorbance (middle) and light-scattering counts (bottom, mean  $\pm$  s.d. ( $n=5$ )) are shown acquired while cooling solutions of 6 in wet, as-received or dry MCH. **b**, Typical AFM picture (left) and height profiles (right) of a sample of

6 ( $30 \mu\text{M}$  in wet MCH) that was drop-cast on mica in a water-saturated environment. The indicated zone is depicted in Fig. 4d. **c**, Typical AFM picture (left) and height profiles (right) of a sample of 6 ( $30 \mu\text{M}$  in dry MCH) that was drop-cast on mica under dry conditions in a glovebox. The indicated zone is depicted in Fig. 4e.